Journal of
Materials Chemistry A

PAPER

View Article Online
View Journal | View Issue

Cite this: *J. Mater. Chem. A*, 2019, **7**, 24614

A zinc(II) complex of di(naphthylethynyl) azadipyrromethene with low synthetic complexity leads to OPV with high industrial accessibility†

Chunlai Wang,[a] Peiran Wei,[a] Jenner H. L. Ngai,[b] Arnold L. Rheingold,[c] Thomas G. Gray,[a] Yuning Li,[b] Emily Pentzer,[a] Ruipeng Li,[d] Lei Zhu[e] and Geneviève Sauvé*[a]

Received 7th August 2019
Accepted 4th October 2019

DOI: 10.1039/c9ta08654d

rsc.li/materials-a

Organic photovoltaics have reached high power conversion efficiencies (PCE) using non-fullerene acceptors (NFAs). However, the best NFAs tend to have complex syntheses, limiting scalability. Among polymer donors, regioregular poly(3-hexylthiophene) (P3HT) has the greatest potential for commercialization due to its simple synthesis and good stability, but PCEs have been limited. It is thus imperative to find scalable NFAs that give high PCE with P3HT. We report a zinc(II) complex of di(naphthylethynyl)azadipyrromethene ($Zn(L2)_2$) as a non-planar NFA that can be synthesized on the gram scale using inexpensive starting materials without chromatography column purification. The NFA has strong absorption in the 600–800 nm region. Time-dependent density-functional theory calculations suggest that the low-energy absorptions can be understood within a four-orbital model involving transitions between π-orbitals on the azadipyrromethene core. OPVs fabricated from P3HT:$Zn(L2)_2$ blends reached a PCE of 5.5%, and the PCE was not very sensitive to the P3HT:$Zn(L2)_2$ weight ratio. Due to its shape, $Zn(L2)_2$ shows isotropic charge transport and its potential as an electron donor is also demonstrated. The combination of simple synthesis, good PCE and photostability, and tolerance to the active material weight ratio demonstrates the potential of $Zn(L2)_2$ as an active layer material in OPVs.

Introduction

Solution processed organic photovoltaics (OPVs) are promising devices for the conversion of solar energy into electricity due to their attractive properties of low-cost, light weight, flexibility, aesthetic appearance (colored or semitransparent) and non-toxicity.[1–3] The active layer of OPVs typically consists of a blend of two conjugated compounds: an electron donor and an electron acceptor. Until recently, fullerene-derivatives were favored as electron acceptors, but it became clear that using fullerene-derivatives as acceptors severely limits device performance, stability and mechanical flexibility. This drove research in the synthesis and application of non-fullerene acceptors (NFAs). Research over the last decade has demonstrated that NFAs are promising for overcoming many of these limitations, with PCEs for single junction OPVs reaching 16%,[4–11] and reports of better mechanical properties and stability.[12–16] However, most of the research on active materials has aimed at improving PCE, often without considering other important factors required for commercialization, such as cost and synthetic scalability.[17] As a result, most high-performance donor and acceptor materials contain pricy building blocks or have high synthetic complexity.[18–20] This is an important issue considering that the overall cost of an OPV technology heavily depends on the material cost.[20]

Estimating the industrial cost and scalability of active layer materials is difficult. Pellegrino and co-workers proposed a more convenient but indirect way to estimate cost by calculating the synthetic complexity (SC), assessed using five parameters: number of synthetic steps (NSS), reciprocal yield (RY), number of operation units for isolation or purification (NUO), number of chromatography columns (NCC) and number of hazardous chemicals (NHC).[18] Each parameter is related to the maximum number obtained from a list of 92 high

---

[a] *Department of Chemistry, Case Western Reserve University, Cleveland, Ohio 44106-7078, USA. E-mail: genevieve.sauve@case.edu*

[b] *Department of Chemical Engineering and Waterloo Institute for Nanotechnology (WIN), University of Waterloo, Waterloo, Ontario, N2L 3G1, Canada*

[c] *Department of Chemistry and Biochemistry, University of California, La Jolla, San Diego, California 92093, USA*

[d] *National Synchrotron Light Source II, Brookhaven National Laboratory, Upon, New York 11973, USA*

[e] *Department of Macromolecular Science and Engineering, Case Western Reserve University, Cleveland, Ohio 44106-7202, USA*

† Electronic supplementary information (ESI) available. 1916509 and 1916510. For ESI and crystallographic data in CIF or other electronic format see DOI: 10.1039/c9ta08654d

performance conjugated polymer donors analyzed, and weighted for its importance using the following equation:

$$\mathrm{SC} = 35\frac{\mathrm{NSS}}{\mathrm{NSS_{max}}} + 25\frac{\log \mathrm{RY}}{\log \mathrm{RY_{max}}} + 15\frac{\mathrm{NUO}}{\mathrm{NUO_{max}}} + 15\frac{\mathrm{NCC}}{\mathrm{NCC_{max}}} + 10\frac{\mathrm{NHC}}{\mathrm{NHC_{max}}} \quad (1)$$

The obtained SC is therefore a percentage relative to a maximum number, and the lower the percentage, the better. Regioregular poly(3-hexylthiophene) (P3HT) had by far the lowest SC of the 92 polymer donors analyzed, at 7.7%. For comparison, the higher performance polymer polythieno[3,4-*b*]-thiophene-*co*-benzodithiophene (PTB7) has a SC of 58%. For electron acceptors, only a few SC indexes are reported, and they also tend to be high. For example, phenyl-C_{61}-butyric acid methyl ester (PCBM) has the lowest SC at ~20%. The high performance NFA 3,9-bis(2-methylene-(3-(1,1-dicyanomethylene)-indanone))-5,5,11,11-tetrakis(4-hexylphenyl)-dithieno[2,3-*d*:2′,3′-*d*′]-*s*-indaceno[1,2-*b*:5,6-*b*′]dithiophene (ITIC) has a SC of ~57%.[20,21] Low SC materials tend to have a simple structure and straightforward synthesis, such as P3HT. It is not surprising that P3HT is currently the only high-efficiency polymer donor that is available on a large scale (>10 kg).[17]

Recently, a high performance solar cell was reported to use low cost materials: (poly{(thiophene)-*alt*-[6,7-difluoro-2-(2 hexyldecyloxy)quinoxaline]} (PTQ10) as the donor and 6-fluoro-[3-(1,1-dicyanomethylene)-indanone]-4,4,9,9-tetrahexyl-5,10-dimethoxyl-4,9-dihydro-*s*-indaceno [1,2-*b*:5,6-*b*′] dithiophene (MO-IDIC-2F)) as the acceptor.[5,22] Their cost calculation is based on the cost of chemicals and solvents, but does not take into account labor costs. For better comparison, we calculated the SC of the two materials using the reported experimental details and obtained 14.8% for PTQ10 and 25.2% for MO-IDIC-2F (see Tables S10 and S11†).

To better evaluate the potential of an active layer blend for commercialization, it is also important to consider solar cell performance and stability.[18,20,23] A new index, called the industrial figure of merit (i-FoM), considers these factors and can be calculate using the equation:

$$\text{i-FoM} = \frac{\mathrm{PCE} \times \text{photostability}}{\mathrm{SC}} \quad (2)$$

where the photostability data are from a normal device under illumination and an inert atmosphere for 200 h.[20] Using this equation, the higher the number, the better the overall performance. In the best case scenario, Li, Brabec and co-workers estimated that if a blend had as low a SC as P3HT:PCBM but also a photostability of 1.0 and a maximum theoretical efficiency of 19.8%, a high i-FoM of 1.3 would be obtained.[23] The authors proposed a benchmark i-FoM of 0.7 using a PCE of 10% and a photostability of 0.98. The i-FoM for the blend with the lowest SC, P3HT:PCBM, is only 0.18 due to the low PCE of 2.8%. On the other hand, by replacing P3HT with the high performance poly[(5,6-difluoro-2,1,3-benzothiadiazol-4,7-diyl)-*alt*-(3,3‴-di(2-octyldodecyl)-2,2′;5′,2″;5″,2‴-quaterthiophen-5,5‴-diyl)] (PCE11), the PCE increased to 9.2%, but the i-FoM only increased to 0.26 due to the high SC of the PCE11:PCBM blend. The i-FoM of the recently reported PTQ10:Mo-IDIC-2F blend has not been reported and cannot be calculated because the photostability is not reported. However, if we assumed a photostability of 0.8, an i-FoM of 0.5 would be obtained, illustrating the importance of lowering SC while maximizing PCE to increase i-FoM.

We note that to obtain the highest theoretical PCE of 19.8%, Li, Brabec and co-workers found that the hypothetical NFA should have a bandgap of 1.4 eV while the polymer donor bandgap can range from 1.6 to 1.9 eV, *i.e.*, it was not sensitive to the polymer donor's bandgap. In this case, the preferred polymer donor for commercialization would therefore be the one with good photostability and low SC, such as P3HT. To our knowledge, the highest PCE for a P3HT based OPV is 6.4%,[13] but the i-FoM is only 0.23 due to the high SC of the NFA. We therefore favor developing novel NFAs that have low SC and that give high PCE and photostability when blended with P3HT.

In the past, we reported a promising class of NFAs based on homoleptic zinc(II) complexes of di(phenylethynyl)azadipyrromethene, $\mathrm{Zn(WS3)_2}$ in Fig. 1.[24,25] This complex has high electron affinity and high absorption between 600 and 800 nm, complementary to P3HT. The non-planarity of the complex contributes to favorable nanoscale phase separation from P3HT. Moreover, these complexes are relatively easy to synthesize from cheap and readily accessible starting materials. However, P3HT:$\mathrm{Zn(WS3)_2}$ typically have a PCE of around 2.5%, too low for practical applications.[26,27] Substituting the pyrrolic phenylethynyl groups with thiophene, thienylethynyl or styryl groups have not improved the performance.[28,29] On the other hand, fluorination at the *para* position of the phenylethynyls improved the PCE to 3.7% and significantly increased the electron mobility.[26] The only crystal structure of a $\mathrm{Zn(WS3)_2}$ derivative we had prior to this report was that of the complex with F at the *para* distal phenyls, and it showed intermolecular interactions between the pyrrolic phenyls of two neighboring molecules.[30] Based on these results, we hypothesized that the aromatic group on the pyrrolic substituent plays an important role in charge transport.

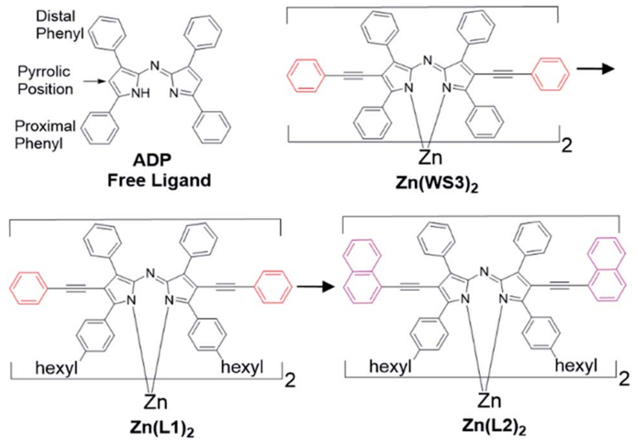

Fig. 1 Chemical Structure of ADP and zinc(II) complexes.

To test this hypothesis, we replaced the phenyl in the pyrrolic phenylethynyl groups with a larger aromatic group in order to enhance intermolecular π–π interactions and charge transport. Naphthalene was chosen because the starting material is inexpensive and readily available. After a few synthetic experiments, it became apparent that replacing the phenyl units with naphthyl groups significantly reduced solubility in organic solvents. It was therefore necessary to add solubilizing groups. Herein, we report the synthesis and properties of two new complexes: $Zn(L1)_2$ and $Zn(L2)_2$ (see Fig. 1). $Zn(L1)_2$ is derived from $Zn(WS3)_2$ with hexyl groups at the *para* position of the proximal phenyls. $Zn(L2)_2$ is derived from $Zn(L1)_2$ with 1-naphthylethynyl groups at the pyrrolic positions. The complexes were fully characterized and tested in OPVs using P3HT as the donor. $Zn(L2)_2$ exhibits interesting properties such as ambipolarity and isotropic charge transport. Moreover, the SC of $Zn(L2)_2$ was calculated to be 22.1%, which is lower than that of most existing high performance NFAs, and when combined with an OPV PCE of 5.5% and 200 h photostability of 81%, a high i-FoM of 0.30 was achieved, getting closer to the benchmark of 0.7 thought to be required for commercialization.

Results and discussion

Synthesis

Scheme 1 summarizes the synthesis of $Zn(L1)_2$ and $Zn(L2)_2$. First, the ADP ligand with proximal (abbreviated as *pr*) hexyl solubilizing groups (*pr*-hexylADP) was synthesized from appropriate hexyl-functionalized starting materials.[31] In order to install pyrrolic substituents, the ligand was then iodinated to obtain a dark blue product, *pr*-hexylADPI$_2$.[28,30] Pyrrolic substituents were installed by reacting appropriate tributyl tin compounds with *pr*-hexylADPI$_2$ using Stille coupling conditions.[28] The reaction was monitored using MALDI-TOF MS and found to be complete in about 6 h, much less time than the 48 h required for the completion of the synthesis of iodinated ligands without hexyl groups.[28,30] This faster reaction time is thought to be due to the improved solubility of the free ligands with hexyl groups. The ligands L1 and L2 were purified by washing with methanol and were isolated as dark blue powders in very good yields (~90%). L1 and L2 were slightly soluble in non-polar solvents, such as hexanes, and readily soluble in polar solvents, such as acetone and dichloromethane.

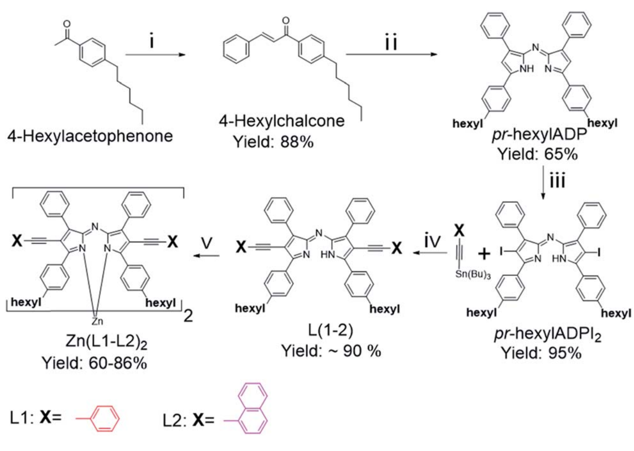

Scheme 1 Synthesis scheme for zinc(II) complexes: $Zn(L1)_2$ and $Zn(L2)_2$. (i) MeOH, 5 M NaOH, 25 °C, 24 h; (ii) $MeNO_2$, DEA, MeOH, reflux, 24 h; ammonium acetate, 1-butanol, reflux, 24 h; (iii) NIS, $CHCl_3$, acetic acid, 25 °C, 12 h under dark conditions; (iv) $Pd(PPh_3)_4$, xylenes, 125 °C, 8 h; (v) THF, NaH, 55 °C, 4 h, followed by CH_2Cl_2, $ZnCl_2$/MeOH, 25 °C, 24 h.

The zinc(II) complexes were synthesized using our published procedure in good yields.[30] Both $Zn(L1)_2$ and $Zn(L2)_2$ were easier to purify than Zn(WS3), which contains no hexyl groups. $Zn(L1)_2$ still required column chromatography to obtain a pure product, but a shorter column (~8 inch) was required than for other $Zn(WS3)_2$ derivatives (~15 inch) due to the higher solubility and lower polarity of $Zn(L1)_2$. The product $Zn(L1)_2$ was collected from the first blue colored fraction, and the yield of $Zn(L1)_2$, 61%, was higher than the yield of $Zn(WS3)_2$, 54%.[28] In contrast, $Zn(L2)_2$ did not require any column to obtain a pure compound. Instead, pure $Zn(L2)_2$ was obtained by washing the product with methanol to remove salt and polar impurities, and acetone to remove the unreacted ligand. $Zn(L2)_2$ was then extracted with dichloromethane to give a dark blue solid in 86% yield. The high yield of $Zn(L2)_2$ was attributed to the easy purification method. The identity and purity of the complexes were confirmed by ^1H NMR, MADI-TOF MS and elemental analysis (see the ESI†). The combination of easy synthesis from readily accessible building blocks with no column chromatography required enables easier scale up of $Zn(L2)_2$ than most existing non-fullerene acceptors.

Optical and electrochemical properties

The UV-Vis absorption spectra of $Zn(L1)_2$ and $Zn(L2)_2$ in chloroform are shown in Fig. 2 and summarized in Table 1. The spectrum of $Zn(WS3)_2$ is included for comparison. The spectrum of $Zn(L1)_2$ is similar to that of $Zn(WS3)_2$, but the visible band is red-shifted by ~5 nm to a λ_{max} of 679 nm due to the electron donating hexyl groups, and the absorptivity (ε_1) increases from 1.21×10^5 M^{-1} cm^{-1} at a λ_{max} of 674 nm for $Zn(WS3)_2$ to 1.35×10^5 M^{-1} cm^{-1} at a λ_{max} of 679 nm for $Zn(L1)_2$. The spectrum of $Zn(L2)_2$ is also similar to that of $Zn(WS3)_2$ but is further red-shifted to a λ_{max} of 700 nm and the absorptivity of the visible band increases to 1.43×10^5 M^{-1} cm^{-1}, most likely due to the larger conjugated length of $Zn(L2)_2$. A similar trend in λ_{max} was observed for the film absorption spectra (Fig. S16a†), with λ_{max} increasing from 701 nm for $Zn(WS3)_2$ to 716 and 727 nm for $Zn(L1)_2$ and $Zn(L2)_2$, respectively. Absorption coefficients for all zinc complexes were similar, at ~2.1×10^5 cm^{-1} (Table S16b†). Table 1 reports the red-shift of the λ_{max} observed upon film formation. All complexes red-shifted upon film formation, suggesting increased intermolecular interactions in the solid state. Interestingly, the λ_{max} of $Zn(L1)_2$ red-shifts 37 nm in films compared to 27 nm for both $Zn(WS3)_2$ and $Zn(L2)_2$, suggesting that hexyl groups on the proximal phenyl rings induced more intermolecular interactions in $Zn(L1)_2$. The cyclic voltammograms (CV) of the zinc(II) complexes in dichloromethane are shown in

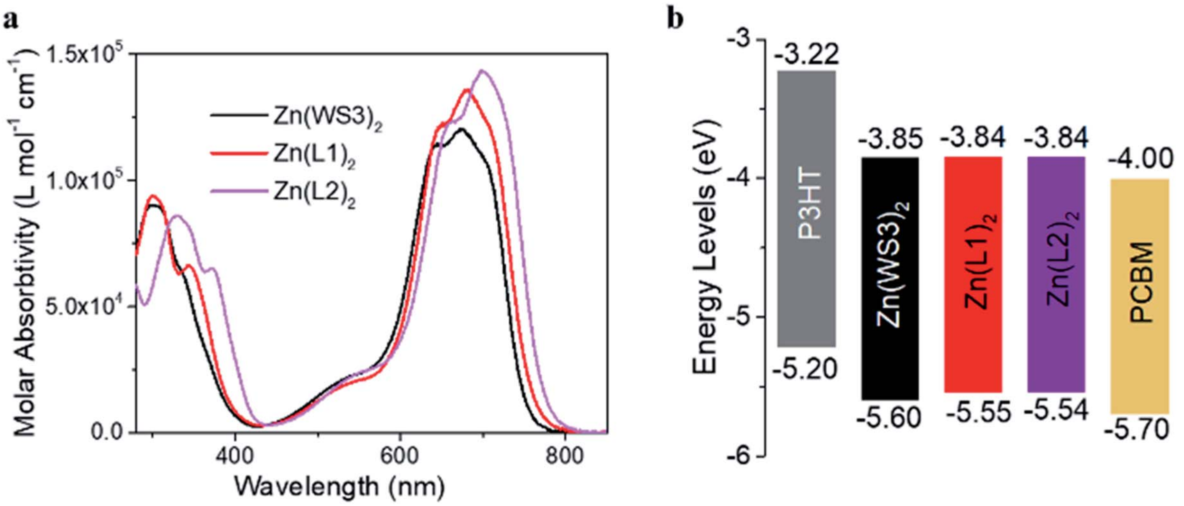

Fig. 2 (a) UV-Vis absorption spectra of zinc(II) complexes in chloroform. (b) Estimated HOMO and LUMO energy levels obtained by cyclic voltammetry. The energy levels for P3HT were estimated using the oxidation onset in films and optical gap.[45] The energy levels of all molecular electron acceptors were obtained under the same conditions in our laboratory, from the $E_{1/2}$ values in dichloromethane and using the value of −5.1 eV for Fc/Fc$^+$.[24]

Fig. S18† and summarized in Table S1.† The CV of PCBM obtained in our laboratory under the same conditions is also included for comparison. The CVs of Zn(L1)$_2$ and Zn(L2)$_2$ are similar to that of Zn(WS3)$_2$, with two reversible oxidation and two reversible reduction peaks. Fig. 2b summarizes the estimated HOMO and LUMO energy levels obtained from the $E_{1/2}$ values of the first oxidation and first reduction peaks, respectively. Both Zn(L1)$_2$ and Zn(L2)$_2$ have very similar LUMO energy levels to Zn(WS3)$_2$, whereas the estimated HOMO levels were a bit higher than that of Zn(WS3)$_2$, by 0.05 and 0.06 eV for Zn(L1)$_2$ and Zn(L2)$_2$, respectively. These small estimated energy level changes are unlikely to have any significant impact on device performance when using P3HT as the donor.

Thermal properties

The thermal stability of the zinc(II) complexes was investigated by thermal gravimetric analysis (TGA). The thermographs are shown in Fig. S17.† All zinc(II) complexes were thermally stable, with a 5% weight loss temperature (T5%) of 462, 454 and 415 °C for Zn(WS3)$_2$, Zn(L1)$_2$ and Zn(L2)$_2$, respectively. While the hexyl groups had little impact on the stability of the complexes, the substitution of phenyl with naphthyl groups slightly reduced T5%. Nevertheless, these T5% values are sufficiently high for most device fabrication conditions.

Fig. 3 shows the differential scanning calorimetry (DSC) profiles of the first heating cycle for P3HT, zinc(II) complexes, and blends of zinc(II) complexes with P3HT. The first cooling cycle and subsequent heating/cooling cycles are featureless. For neat films, Zn(L1)$_2$ and Zn(L2)$_2$ both showed an exothermic peak during the first heating cycle at 210 °C (enthalpy $\Delta H_f = 33$ J g^{-1}) and 229 °C ($\Delta H_f = 44$ J g^{-1}), respectively, and no peaks during the cooling cycle. These results are consistent with crystalline Zn(L1)$_2$ and Zn(L2)$_2$ melting into an isotropic liquid upon heating, followed by glass formation upon cooling.[32] Conventional melting point measurements confirmed that the exothermic peak for Zn(L1)$_2$ and Zn(L2)$_2$ represents a crystal-melting phase transition (see Fig. S19†). On the other hand, Zn(WS3)$_2$ exhibits no peaks upon heating and cooling in the 25–300 °C temperature range. This suggests that the hexyl groups increase the crystallinity of zinc(II) complexes. The substitution

Table 1 Summary of the optical properties of zinc(II) complexes in solution and film

	Solution		Film			
Zinc(II) complexes	λ_{max} (nm) (ε_1, ×10^3 M^{-1} cm^{-1}, ε_2, ×L g^{-1} cm^{-1})	λ_{onset} (nm)	λ_{max} (nm) (absorption coefficient α, ×10^5 cm^{-1})	λ_{onset} (nm)	Optical gap (eV)	$\Delta\lambda_{max}$ upon film formation
Zn(WS3)$_2$	300 (90, 66), 645 (114, 84), 674 (121, 89)	753	701 (2.14)	791	1.57	27
Zn(L1)$_2$	300 (94, 55), 344 (66, 39), 650 (122, 72), 679 (135, 79)	760	716 (2.11)	801	1.55	37
Zn(L2)$_2$	330 (86, 45), 373 (65, 34), 664 (123, 65), 700 (143, 75)	775	727 (2.13)	805	1.54	27

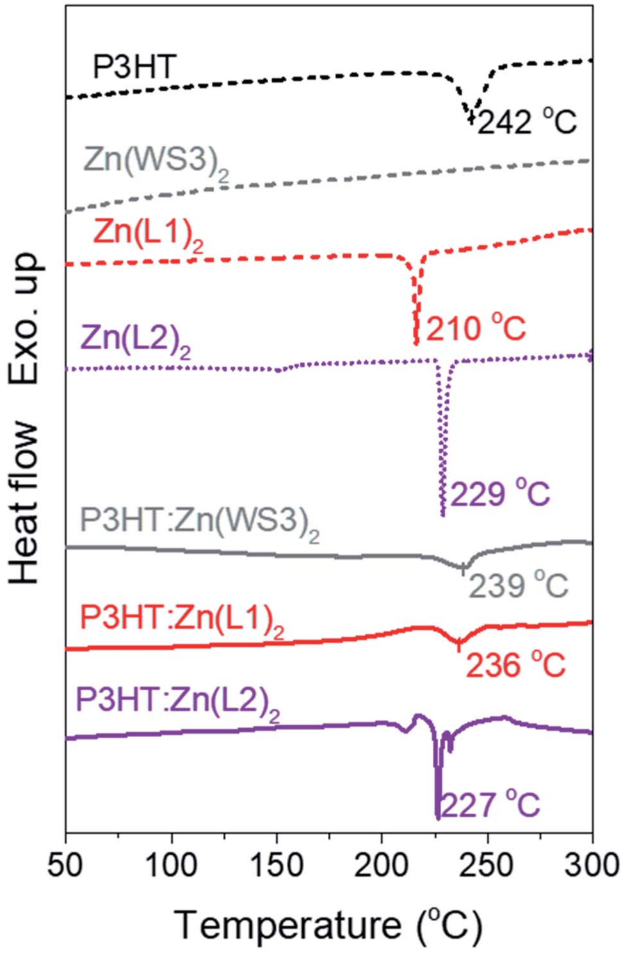

Fig. 3 DSC curves for the zinc(II) complexes and P3HT:zinc(II) complex blends in the first heating cycle. The blend ratios are the same as the optimized ratios in OPVs.

of phenyl groups in Zn(L1)$_2$ with naphthyl groups (Zn(L2)$_2$) further increased crystallinity because the melting temperature and ΔH_f increased by 19 °C and 11 J g^{-1}, respectively.

In blend films, a broad exothermic peak in the 235–239 °C range is assigned to melting of P3HT. These temperatures are slightly lower than the melting temperature of neat P3HT at 242 °C. The calculated ΔH_f for P3HT in neat P3HT, P3HT:Zn(WS3)$_2$, P3HT:Zn(L1)$_2$ and P3HT:Zn(L2)$_2$ is 21, 19, 17, and 17 J g^{-1}, respectively. The lower melting temperature and ΔH_f of P3HT in blends indicate that all zinc(II) complexes interfere slightly with P3HT crystallization. In addition, Zn(L2)$_2$ is the only zinc(II) complex that shows a melting transition in blends (at 227 °C), indicating that it is the only complex that remains crystalline in blends with P3HT.

Crystallography

Both Zn(L1)$_2$ and Zn(L2)$_2$ were successfully crystallized by dissolving the complexes in a solvent mixture of dichloromethane and acetonitrile with a volume ratio of 8 : 1, followed by slow evaporation of dichloromethane from the mixture. The crystals were large, diamond-shaped and dark purple in color (see Fig. S21†). On the other hand, multiple attempts to crystallize Zn(WS3)$_2$ only resulted in very small needle-shaped crystals, which were not suitable for single crystal structure determination. Since the only structural difference between Zn(L1)$_2$ and Zn(WS3)$_2$ is the hexyl groups on the proximal phenyls, it is likely that the hexyl groups facilitate the molecular packing and thus the crystallization of zinc(II) complexes, consistent with the DSC results above. Without the hexyl groups, Zn(WS3)$_2$ is a good glass-former because it is too rigid to pack into a long range order. Fig. 4 shows the ellipsoid plot of Zn(L1)$_2$ and Zn(L2)$_2$. Similar to Zn(ADP)$_2$, the zinc(II) complexes exhibit a distorted tetrahedral structure with intra-molecular π–π stacking in four places between a proximal phenyl of one ligand and a pyrrole ring of the other ligand. Zn(L2)$_2$ exhibits a larger dihedral angle, 72.2°, and a smaller intra-molecular π–π stacking distance (3.73 Å) than Zn(L1)$_2$, which has a dihedral angle of 70.7° and π–π stacking distance of 3.82 Å. The shorter π–π stacking distance for Zn(L2)$_2$ suggests a stronger intra-molecular interaction between the proximal phenyl and pyrrole rings. Moreover, Zn(L1)$_2$ and Zn(L2)$_2$ show different crystal packing depending on the aryl groups used on the pyrrolic acetylene positions, see Fig. S21.† Zn(L1)$_2$ has a T-shape inter-molecular interaction between distal and pyrrolic phenyl rings and a parallel interaction between proximal phenyls. On the other hand, Zn(L2)$_2$ prefer a T-shape inter-molecular interaction between the

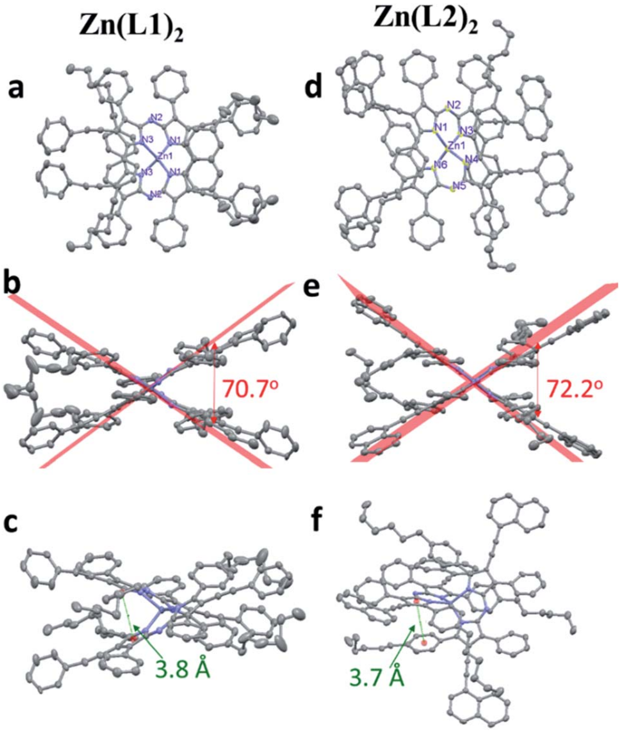

Fig. 4 Ellipsoid plot of Zn(L1)$_2$ and Zn(L2)$_2$. The hydrogen atoms and dichloromethane solvate were omitted for clarity. (a) and (d) show the structure of Zn(L1)$_2$ and Zn(L2)$_2$, respectively; (b) and (e) show the distorted tetrahedral shape; (c) and (f) show the intramolecular π–π stacking between the proximal phenyl group of one ligand and a core (pyrrole ring) of the other ligand. Distance was measured between the centroids of the rings.

pyrrolic naphthyls and the distal phenyls and another T-shape interaction between the pyrrolic naphthyls and the pyrrole rings in the core. The inter- and intra-molecular interacting properties of these zinc(II) complexes are summarized in Table 2. This demonstrates that the nature of the aryl group has a strong influence on ligand arrangement and self-assembly in the solid state. In addition, these zinc(II) complexes exhibit 3D π–π interactions in the crystal.

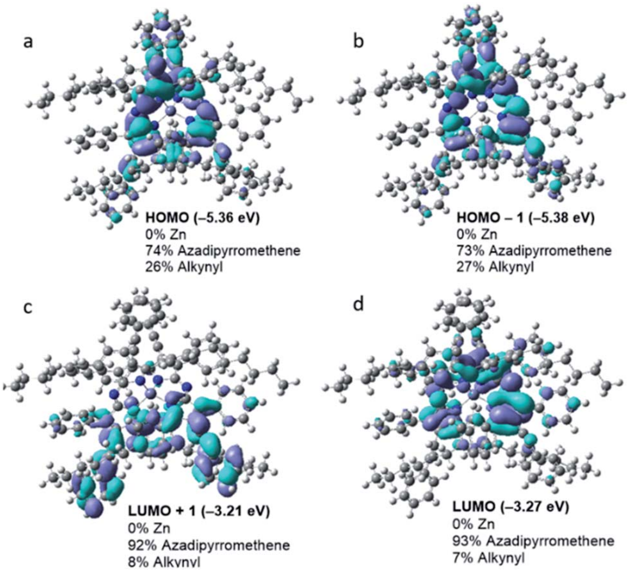

Fig. 5 Plots of the (a) HOMO, (b) HOMO−1, (c) LUMO+1 and (d) LUMO of Zn(L1)$_2$ (contour level 0.02 a.u.). Orbital compositions are expressed as percentages of electron density.

Calculations

The electronic structures of Zn(L1)$_2$ and Zn(L2)$_2$ were investigated with density-functional theory (DFT) calculations. Unconstrained geometry optimization converged to local minima of the potential energy hypersurfaces, as verified by harmonic vibrational frequency analyses. Calculated metrics are in good agreement with crystallographic values. The average zinc(II)-nitrogen bond lengths are 1.93 Å (experimental 1.99 Å) for Zn(L1)$_2$ and 2.01 Å (experimental 2.01 Å) for Zn(L2)$_2$. A noteworthy feature of the structure of each complex is the distorted tetrahedral geometry of zinc(II). For Zn(L1)$_2$, the computed angle between chelate N–Zn–N planes is 84.4° (75.3°, experimental); for Zn(L2)$_2$, this angle is 85.1° (74.8°, experimental). Thus, gas-phase geometry optimization captures the flattened structure of the complexes, despite the absence of ligand-field stabilization for zinc(II) (d10).

Fig. 5 shows the contour plots of four Frontier orbitals of Zn(L1)$_2$. The two highest occupied Kohn–Sham orbitals (HOMOs) are quasi-degenerate, as are the first two lowest unoccupied Kohn–Sham orbitals (LUMOs). All four orbitals are delocalized over both ligands, with minimal participation of zinc(II). For both HOMOs and both LUMOs, the greater part of each orbital resides on the tetraphenyl azadipyrromethene moiety, and contributions from the arylalkynyl substituents are substantial. The *n*-hexyl substituents participate negligibly. Similar results are observed from the Frontier orbitals of Zn(L2)$_2$, see Fig. S22.†

Time-dependent DFT calculations were performed on the first 40 Franck–Condon singlet states of both complexes. The low-energy absorption spectra of Zn(L1)$_2$ and Zn(L2)$_2$ can be rationalized in terms of a four-orbital model involving single-particle excitations from the two HOMOs to the two LUMOs. Fig. 6 shows a state diagram depicting the relevant transitions for Zn(L1)$_2$. All four transitions in the figure engage in configuration interaction; the figure indicates the major contributors to each state. The first two Frank–Condon singlets have minuscule oscillator strengths, 0.018 and 0.016, respectively, for Zn(L1)$_2$. These transitions contribute sparingly to the absorption onset. The oscillator strengths of the third and fourth transitions are much higher, 0.88 and 1.2 respectively. Together, these transitions account for the major absorptions at 650 and 679 nm for Zn(L1)$_2$, and for the complex's intense blue color. Similar results are obtained for Zn(L2)$_2$, and a four-state diagram is reproduced as shown in Fig. S23.† These results agree with earlier calculations on bis(azadipyrromethenes) of zinc(II),[33] and mono(azadipyrromethene) complexes of other d10 metal ions.[34–36] The changes in orbital compositions between the two highest occupied and two lowest unoccupied orbitals (indicated in Fig. 5) suggest a degree of charge transfer from the alkynyls to the azadipyrromethene in these intraligand π–π* transitions.

Photovoltaic properties

Photovoltaic properties were investigated using an inverted configuration: ITO/ZnO/P3HT:acceptor/MoO$_3$/Ag. Device processing optimization involved screening for appropriate donor-

Table 2 Summary of inter- and intra-molecular interactions of zinc(II) complexes[a]

Zn complexes	Intramol. dihedral angle (°)	Intramol. π–π stacking distance (Å)	Intermol. π–π stacking type	Intermol. π–π stacking distance (Å)
Zn(L1)$_2$	70.7	3.82	Distal-pyrrolic (T) and proximal–proximal (P)	4.34, 4.83
Zn(L2)$_2$	72.2	3.73	Pyrrolic-core (T) and pyrrolic-distal (T)	4.78, 4.42

[a] Distal, proximal, pyrrolic and core mean the distal phenyl ring, proximal phenyl ring, pyrrolic phenyl ring and pyrrole ring, respectively. Intermolecular π–π stacking types are sandwich (S), T-shaped (T) and parallel (P) π–π stacking.

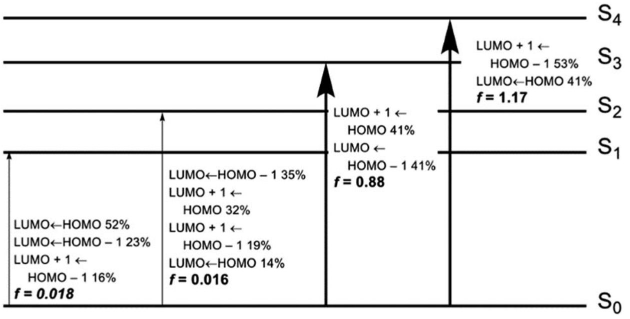

Fig. 6 Lowest-lying Franck–Condon singlet excited states of $Zn(L1)_2$ (energies not shown to scale). Percentage composition of vertical transitions and oscillator strengths are indicated to the right of each arrow.

to-acceptor blend weight ratios, total concentration, and annealing conditions; optimization details are summarized in Tables S2–S8.† Fig. 7a shows the current density–voltage curves of the best devices, and the performance parameters are summarized in Table 3. The best PCE obtained was 2.5%, 3.0% and 5.5% for $Zn(WS3)_2$, $Zn(L1)_2$ and $Zn(L2)_2$, respectively. The 5.5% PCE of the $Zn(L2)_2$ cell is amongst the best reported performances for P3HT-based OPVs, due to its high V_{OC}, J_{SC} and FF being 0.83 V, 11.3 mA cm^{-2} and 59%, respectively. In addition, the $Zn(L2)_2$ cell performance was much less sensitive to the donor : acceptor ratio than for other zinc(II) complexes: for example, the PCE of $Zn(L2)_2$ cells ranged between 4.1% and 5.4% for ratios of 1 : 0.5 to 1 : 1.5 (Table S5†), whereas the PCE of $Zn(L1)_2$ ranged between 1.4% and 2.4% for ratios of 1 : 0.6 to 1 : 1.1 (Table S2†). The low sensitivity of $Zn(L2)_2$ performance to the donor : acceptor ratio should be advantageous for commercialization.

To better understand the PCE differences, we analyzed the device performance parameters. All zinc(II) complex cells have higher open-circuit voltages (V_{OC}, ~0.8 V) than the reference PCBM cell (0.54 V), partly due to the higher LUMO energy level of the zinc(II) complexes. The V_{OC} difference was higher than the difference between the Zn complexes and PCBM energy levels, suggesting that there are less energy losses in the non-fullerene cells. More accurate determination of the LUMO energy levels in films is required to confirm this. The short circuit current (J_{SC}) increased with the introduction of hexyl groups from 5.7 mA cm^{-2} for $Zn(WS3)_2$ to 7.5 mA cm^{-2} for $Zn(L1)_2$. Replacing the

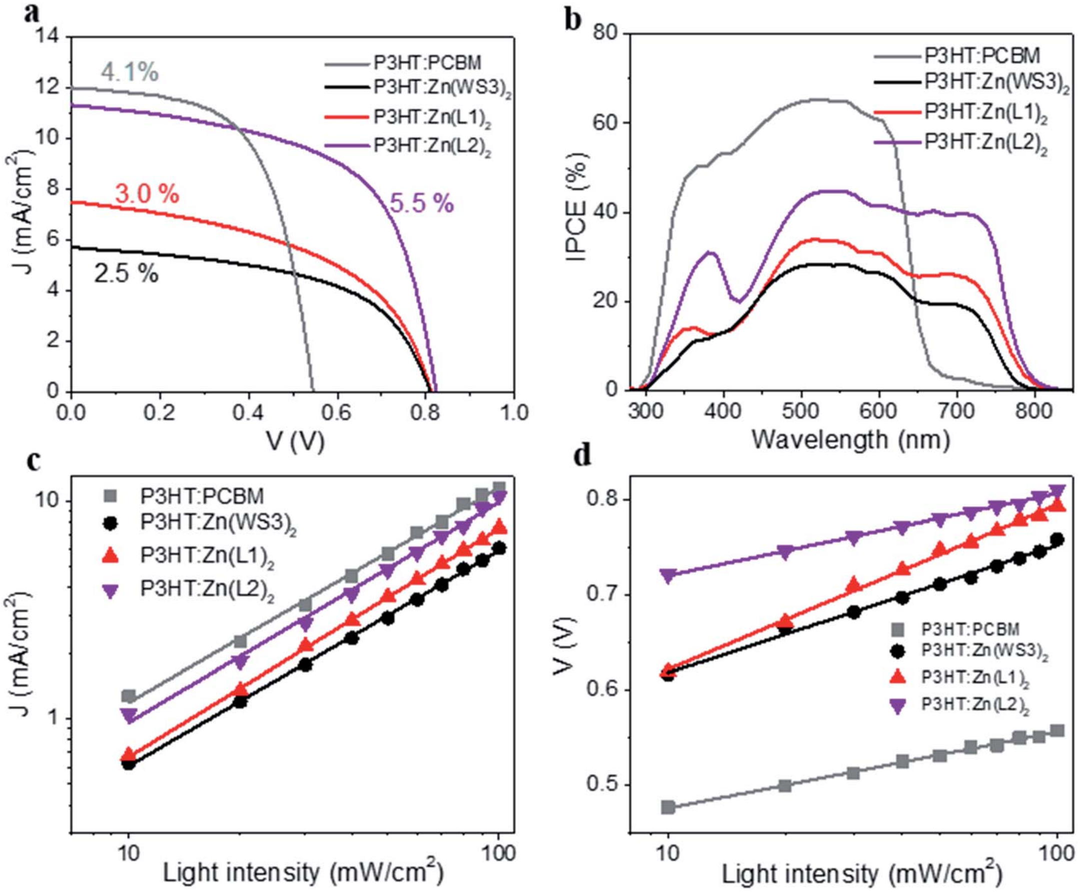

Fig. 7 (a) Current density–voltage characteristics of solar cells with an effective area of 0.2 cm^2 by using simulated AM1.5 G illumination at 100 mW cm^2; (b) incident photon-to-current efficiency (IPCE) spectra of solar cells. (c) J_{SC} as a function of light intensity in a double-logarithmic scale and (d) V_{OC} as a function of light intensity in a semi-logarithmic scale. Fill factor for all cells did not change much in the light intensity ranging from 10 to 100 mW cm^{-2}.

Table 3 Performance parameters, power law exponents and V_{oc} slopes of solar cells^a

Acceptor	V_{OC} (V)	J_{SC} (mA cm^{-2})	FF (%)	PCE (%)	Power law exponent	V_{OC} slope (times of kT/q)
$Zn(WS3)_2$	0.81 (0.77 ± 0.03)^a	5.7 (5.4 ± 0.7)^a	55 (52 ± 6)^a	2.5 (2.1 ± 0.4)^a	0.990	2.6
$Zn(L1)_2$	0.81 (0.80 ± 0.03)	7.5 (7.3 ± 0.3)	49 (49 ± 2)	3.0 (2.8 ± 0.2)	1.05	2.0
$Zn(L2)_2$	0.82 (0.82 ± 0.01)	11.3 (10.8 ± 0.7)	59 (59 ± 3)	5.5 (5.2 ± 0.3)	1.01	1.3
PCBM	0.54 (0.54 ± 0.02)	12.0 (11.5 ± 0.6)	63 (63 ± 1)	4.1 (4.0 ± 0.2)	0.988	1.2

[a] For solar cells, all acceptors were tested by blending with P3HT using optimized conditions. Averages were calculated for at least 10 devices. k is Boltzmann's constant, T is the temperature, and q is the elementary charge.

pyrrolic phenyls with naphthyls further increased J_{SC} to 11.3 mA cm^{-2} for $Zn(L2)_2$. These J_{SC} increases cannot be explained by increased absorption alone. Fig. S24† shows the UV-Vis absorption of P3HT:zinc(II) complex blend films made under the same optimized conditions as the active layer in solar cells. All zinc(II) complex blends have a similar absorbance between 450 nm and 800 nm. Although the P3HT:$Zn(L2)_2$ films exhibit a slightly larger absorption in the 640–800 nm region, it is not sufficient to explain the large J_{SC} increase. The J_{SC} increases are consistent with increases in the incident photon-to-current efficiencies (IPCEs, Fig. 7b): the IPCE at 510 nm was 28%, 34% and 44% for $Zn(WS3)_2$, $Zn(L1)_2$ and $Zn(L2)_2$, respectively. The J_{SC} of the $Zn(L2)_2$ cell calculated by integrating the IPCE spectra was 9.9 mA cm^{-2}, which is 12% lower than the measured J_{SC}. This small difference may be due to cell degradation, as the IPCE measurements were done in air instead of in a glove box. The maximum IPCEs for the zinc(II) complex cells are generally lower than those for PCBM cells because the optimized cell thickness of the zinc(II) complex cells is less, ~80 nm, than that of the PCBM cell, ~190 nm, thus limiting absorption for the zinc(II) complex cells. The J_{SC} and IPCE trends observed within the zinc(II) complex series cannot be explained by absorption differences alone and must depend on other factors affecting photocurrent such as exciton splitting, free charge generation and charge carrier recombination.

To further understand the OPV results, charge recombination was investigated using J–V light intensity dependence measurements. Fig. 7c shows the J_{SC} as a function of light intensity on a double-logarithmic scale and the extracted power law exponent for all solar cells is reported in Table 3. All power law exponents were close to unity, indicating that the loss from bimolecular recombination in all optimized cells is small.[37] Fig. 7d shows the V_{OC} as a function of light intensity on a semi-logarithmic scale. There is a monotonic relationship between V_{OC} and light intensity. The data were fitted into a linear function and the extracted slopes, presented as multiples of kT/q, are summarized in Table 3. A slope of one kT/q indicates that only Langevin recombination is present and a higher than kT/q slope means that trap assisted recombination is also present.[37,38] The slope for P3HT:PCBM cells, 1.2 kT/q, is close to the reported data, 1.4 kT/q, for P3HT:PCBM cells under similar fabrication conditions.[39] Since PCBM is a trap-free material, the carrier traps in the P3HT:PCBM cell were mainly induced by P3HT.[40] The slope for $Zn(WS3)_2$, $Zn(L1)_2$, and $Zn(L2)_2$ cells are 2.6, 2.0 and 1.3 times kT/q, respectively, indicating that $Zn(WS3)_2$ has the largest loss from trap assisted recombination, followed by $Zn(L1)_2$ and $Zn(L2)_2$. This is also consistent with the J_{SC} and PCE trends in OPVs, and partially explains the high J_{SC} and high fill factor of $Zn(L2)_2$ cells.[39] The slope of the $Zn(L2)_2$ cell, 1.3 kT/q, is very close to that of the PCBM cell, 1.2 kT/q, suggesting that the carrier traps are mainly induced by P3HT and that $Zn(L2)_2$ may be nearly trap free.

Charge transport properties

To further understand the performance of zinc(II) complex devices, the space-charge-limited-current (SCLC) method was used to measure the charge carrier mobilities of zinc(II) complexes in neat and blend films. Hole mobility (μ_h) measurement used a device structure of ITO/PEDTO:PSS/active layer/MoO_3/Ag and electron mobility (μ_e) measurement used a device structure of ITO/ZnO/active layer/Ca/Al. Mobilities were calculated with the Mott-Gurney law under the trap free SCLC situation.[41] The SCLC graphs are shown in Fig. S25† and the results are summarized in Table 4. The film electron mobility of all neat zinc(II) complexes varied slightly within the same magnitude, ranging from 1.6×10^{-5} to 4.2×10^{-5} cm^2 V^{-1} s^{-1}, which are about an order of magnitude lower than that of high efficiency NFAs. The relatively low electron mobility of zinc(II) complexes limits the film thickness of optimized cells to ~80 nm, thus limiting light absorption and J_{SC} in cells. Interestingly, both $Zn(L1)_2$ and $Zn(WS3)_2$ have similar neat film hole mobility, around 9×10^{-7} cm^2 V^{-1} s^{-1}. This is about two orders of magnitude lower than that of $Zn(L2)_2$, 1.0×10^{-4} cm^2 V^{-1} s^{-1}, which is close to the reported hole mobility of the pristine P3HT film, (1.4–3) $\times 10^{-4}$ cm^2 V^{-1} s^{-1}.[42] This indicates that $Zn(L2)_2$ can not only transport electrons, but the favorable intermolecular interaction in $Zn(L2)_2$ also facilitates hole transport in the neat film. The blend film mobilities of zinc(II) complexes were also studied. After blending with P3HT, $Zn(WS3)_2$ had a one magnitude drop in electron mobility, from 1.6×10^{-5} cm^2 V^{-1} s^{-1} in the neat film to 4.0×10^{-6} cm^2 V^{-1} s^{-1} in the blend film. In contrast, for $Zn(L1)_2$ and $Zn(L2)_2$ electron mobility in blends was similar to that in neat films. This suggests that the hexyl chains help the zinc(II) complexes maintain a favorable phase separation from P3HT to maintain good electron transport in blends. The hole mobility for all P3HT:zinc(II) complex blends was ~3×10^{-4} cm^2 V^{-1} s^{-1}, attributed to the hole transport in P3HT. The imbalance

Table 4 Charge carrier mobility of zinc(II) complexes by using SCLC and TFT methods[a]

	Mobility measured by SCLC				Mobility measured by TFT	
Acceptor	Neat μ_h ($cm^2 V^{-1} s^{-1}$)	Neat μ_e ($cm^2 V^{-1} s^{-1}$)	Blend μ_h ($cm^2 V^{-1} s^{-1}$)	Blend μ_e ($cm^2 V^{-1} s^{-1}$)	Neat μ_h ($cm^2 V^{-1} s^{-1}$)	Neat μ_e ($cm^2 V^{-1} s^{-1}$)
$Zn(WS3)_2$	8.1×10^{-7}	1.6×10^{-5}	2.4×10^{-4}	4.0×10^{-6}	—	2.3×10^{-5}
$Zn(L1)_2$	9.0×10^{-7}	3.2×10^{-5}	3.0×10^{-4}	4.0×10^{-5}	—	4.6×10^{-5}
$Zn(L2)_2$	1.0×10^{-4}	4.2×10^{-5}	3.1×10^{-4}	2.4×10^{-5}	1.3×10^{-4}	6.8×10^{-5}
PCBM	—	5.0×10^{-3b}	5.5×10^{-4b}	2.6×10^{-3b}	—	—

[a] A minimum of 4 devices were made for each mobility measurement and average values are reported. Blend mobilities were measured from blends of acceptors and P3HT using the same fabrication method as the optimized solar cells. [b] Published data.[26]

between electron and hole mobility may also contribute to charge recombination and low FF.

The SCLC method provides insight into the out-of-plane charge transport between the two electrodes. To investigate the in-plane charge transport along the substrate, charge transport in bottom-gate-bottom-contact thin film transistors (TFTs) was measured, see Table 4. The electron mobility was estimated to be 2.3×10^{-5}, 4.6×10^{-5}, and 6.8×10^{-5} $cm^2 V^{-1} s^{-1}$ for $Zn(WS3)_2$, $Zn(L1)_2$ and $Zn(L2)_2$, respectively. These numbers are similar to those obtained in neat films by the SCLC method. This suggests that charge transport is similar in the two directions in the film, and is consistent with our hypothesis that the 3D π–π stacking of zinc(II) complexes enables isotropic charge transport. The hole mobility of $Zn(L2)_2$ films was 1.3×10^{-4} $cm^2 V^{-1} s^{-1}$ in TFTs, very similar to the value of 1.0×10^{-4} $cm^2 V^{-1} s^{-1}$ obtained by the SCLC method, also consistent with isotropic charge transport.

Morphology

The surface morphology of the optimized cell films (annealed) was studied by tapping-mode atomic force microscopy (AFM). The phase and height images of all zinc(II) complex cells are shown in Fig. 8. The height images show that the films are smooth, with surface roughness ranging from 12 to 5 nm. The phase images show more defined features, with lighter and darker parts related to domains having different adhesion and mechanical properties.[43] The two materials appear to be phase separated with irregularly shaped domains of 25 to 50 nm for P3HT:$Zn(WS3)_2$ and P3HT:$Zn(L1)_2$ blends, and 15 to 40 nm for the P3HT:$Zn(L2)_2$ blends. This phase separation should be good for charge transport to electrodes, consistent with the low bimolecular recombination observed. The smaller domain size range observed for the P3HT:$Zn(L2)_2$ blends is expected to be more favorable for exciton splitting and charge generation than the domain size range of the other two blends. The P3HT:$Zn(L2)_2$ blend therefore appears to have the best surface morphology among the three blends, having small enough phase-separated domains for exciton splitting and large enough phase-separated domains for good charge transport to the electrodes.[44]

To gain insight into the crystalline structure and crystal orientation across the films, neat and blend films were analyzed by two-dimensional (2D) grazing-incidence wide-angle X-ray diffraction (GI-WAXD). The 2D GI-WAXD patterns and corresponding intensity profiles along the q_r (in-plane) direction of the annealed films are shown in Fig. 9, and those of the as-cast films can be found in Fig. S30.† Both the as-cast neat films of $Zn(L1)_2$ and $Zn(L2)_2$ were amorphous. Upon annealing, $Zn(L1)_2$ remained amorphous whereas $Zn(L2)_2$ crystallized. The GI-WAXD pattern of the annealed $Zn(L2)_2$ film shows four defined out-of-plane peaks at $q_z \approx 0.40, 0.52, 0.63$, and 0.71 Å^{-1}, and two defined in-plane peaks at $q_r \approx 1.47$ and 1.52 Å^{-1}. These

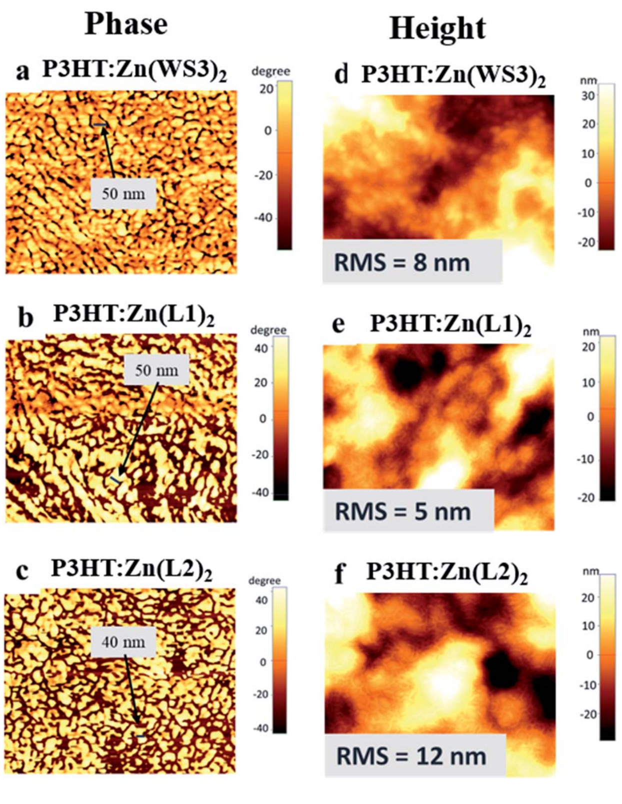

Fig. 8 (a)–(c) Phase images of the optimized OPV films of P3HT:$Zn(WS3)_2$, P3HT:$Zn(L1)_2$ and P3HT:$Zn(L2)_2$, respectively; (d)–(f) height images of P3HT:$Zn(WS3)_2$, P3HT:$Zn(L1)_2$ and P3HT:$Zn(L2)_2$ films respectively. In the phase images, dark and bright parts can be differentiated as different components. All films were annealed under same conditions as the optimized OPVs and all images are 1×1 μm^2.

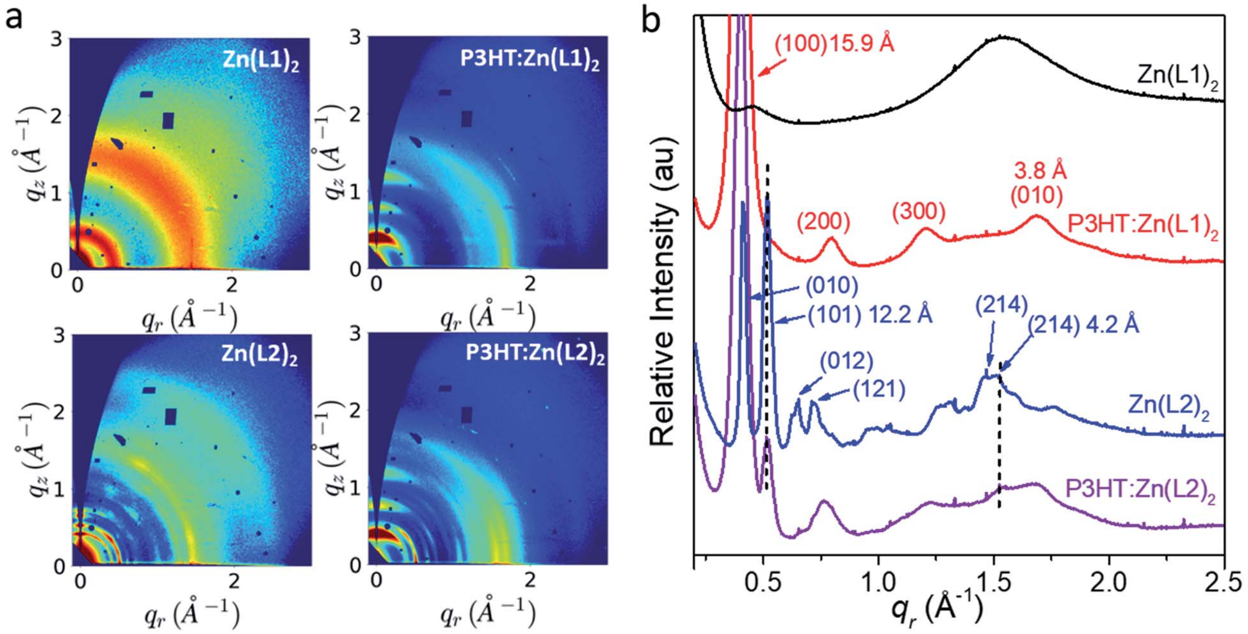

Fig. 9 (a) 2D GI-WAXD patterns of thermally annealed thin films of $Zn(L1)_2$, $Zn(L2)_2$, P3HT:$Zn(L1)_2$ and P3HT:$Zn(L2)_2$. The r and z directions indicate in-plane and out-of-plane directions. The $Zn(L1)_2$ neat and blend films were annealed at 100 °C for 15 min and the $Zn(L2)_2$ films were annealed at 120 °C for 15 min. (b) Corresponding intensity profiles along the q_r axis.

matched well with diffractions in the powder pattern calculated from the single crystals, as labeled in Fig. S29.† The annealed P3HT:$Zn(L1)_2$ blend film shows three orders of out-of-plane (100) lamellar peaks, at $q_z \approx 0.40$, 0.79, and 1.21 Å^{-1}, corresponding to the edge-on orientation of P3HT. An in-plane π–π stacking reflection, (010), was also found at $q_r \approx 1.69$ Å^{-1}, which is consistent with the P3HT crystal structure.[45] This suggests that only P3HT is crystalline in the P3HT:$Zn(L1)_2$ blend films, consistent with the DSC data. The annealed P3HT:$Zn(L2)_2$ blend film shows the P3HT diffraction pattern, indicating that the crystallinity of P3HT was maintained in the blend film. In addition, two defined in-plane diffraction peaks at $q_r \approx 0.52$ and 1.52 Å^{-1} indicated the molecular ordering of $Zn(L2)_2$, consistent with the DSC result that both $Zn(L2)_2$ and P3HT are crystalline in the blend film.

To estimate the crystallite size of P3HT and $Zn(L2)_2$, the GI-WAXD data were analyzed using the Scherrer equation:[46,47]

$$\tau_{hkl} = \lambda \times 0.9/(\beta \cos \theta) \tag{3}$$

where τ_{hkl} is the crystallite size along the $[hkl]$ reflection, λ is the X-ray wavelength and β is the full width at half maximum of the diffraction peak. The diffraction patterns of P3HT and $Zn(L2)_2$ are shown in Fig. S31.† In annealed neat films, the τ_{001} of P3HT and τ_{101} of $Zn(L2)_2$ were estimated to be 12.5 and 13.7 nm, respectively. In the P3HT:$Zn(L2)_2$ annealed blend film, the crystallite size of P3HT decreased slightly to 8.7 nm due to the presence of $Zn(L2)_2$. However, the crystallite size of $Zn(L2)_2$ remained similar in both neat and blend films, at 13.7 nm and 12.3 nm, respectively. These crystallite sizes are favorable for efficient exciton splitting, in agreement with the AFM data presented above.

Donor properties of $Zn(L2)_2$ in OPVs

The SCLC and TFT measurements show that $Zn(L2)_2$ is ambipolar with a well-balanced electron and hole mobility (both electron mobility and hole mobility at around 1×10^{-4} cm^2 V^{-1} s^{-1}). To investigate the electron donating properties of $Zn(L2)_2$ in OPVs, we first attempted to blend $Zn(L2)_2$ with PCBM, but this resulted in uneven films, possibly because both are small molecules with a non-planar shape. To improve the film quality, we then turned to a polymer acceptor that we had available in our laboratory: poly{[*N*,*N*′-bis(2-octyldodecyl)-naphthalene-1,4,5,8-bis(dicarboximide)-2,6-diyl]-*alt*-5,5′-(2,2′-bithiophene)} (P(NDI2OD-T2)) from Polyera. The estimated energy levels for this polymer are lower than those of $Zn(L2)_2$, though the energy offsets are small and not optimal, at ~0.2 and 0.1 eV for LUMOs and HOMOs, respectively (see Fig. S32†). Nevertheless, we fabricated OPVs using the unoptimized conditions: 1 : 1 weight ratio with a total concentration of 25 mg mL^{-1} in *o*-DCB, annealed at 80 °C for 15 min. Preliminary results show a photovoltaic effect with a J_{SC} of 0.084 mA cm^{-2}, a V_{OC} of 0.86 V, a FF of 37% and a PCE of 0.027% (Fig. S32†), demonstrating that $Zn(L2)_2$ has potential as a donor in OPVs. We note that other azadipyrromethene-based dyes have been reported to work as donors with evaporated fullerene (C_{60}) as the acceptor.[48–50] Since the morphology is critical for good performance, the surface morphology of the blend films was imaged by AFM, as shown in Fig. S28.† The domain size appears to be ~12 nm, and the film has a surface roughness of 2.8 nm, with no obvious large-scale phase separation. The low performance is likely due to a combination of unoptimized energy level alignment (see Fig. S32†), non-complementary absorption of the two components (both absorb in UV and between 600 and

800 nm), and low exciton diffusion length of P(NDI2OD-T2) (1.1 nm, much smaller than the 12 nm domain size observed).[51] The 3-D molecular shape and good hole mobility of $Zn(L2)_2$ are expected to enable high performance with a high bandgap polymer acceptor that has a deep LUMO energy level – however, the optimization of the polymer acceptor is required and is beyond the scope of this paper.

Commercial accessibility of P3HT:$Zn(L2)_2$ cells

The synthetic complexity (SC) for $Zn(L1)_2$ and $Zn(L2)_2$ was evaluated by considering the number of synthetic steps, yields, number of purification steps, purifications by column chromatography and number of hazardous chemicals. Details are given in the ESI† section. The SC index was calculated to be 22.9 and 22.1% for $Zn(L1)_2$ and $Zn(L2)_2$, respectively, Tables S10 and S11.† These numbers are close to that of PCBM (20.6%) and lower than those of low-cost NFAs such as MO-IDIC-2F (25.2%, Table S11†) and high performance NFAs such as O-IDTBR (43.9%).[23] Fig. S33† shows the normalized photostability of P3HT:$Zn(L2)_2$ cells in air and under N_2. After 200 h of illumination, the photostability was 81% and 74% in the N_2 atmosphere and in air, respectively. The industrial figure of merit, i-FoM, was calculated from the PCE, photostability under N_2 and SC of the blend.[23] For P3HT:$Zn(L2)_2$, the PCE is 5.5%, the photostability is 0.81 and the SC for the blend is 15%, giving an i-FoM value of 0.30, which is one of the highest i-FoM reported to date.[23] The i-FoM of the PTQ10-MO-IDIC-2F system has not been reported to our knowledge. Assuming a good photostability of 0.8, we estimate an i-FoM value of 0.5, higher than that of our system due to the higher PCE. To increase the commercial accessibility of $Zn(L2)_2$-based solar cells, it is therefore critical to further improve PCE.

Conclusions

Two zinc(II) ADP complexes, $Zn(L1)_2$ and $Zn(L2)_2$, have been successfully synthesized through functionalization of $Zn(WS3)_2$. Both hexyl groups and substitution of phenylethynyl with naphthylethynyl improve the crystallinity of the zinc(II) complexes. Density-functional theory calculations find that the frontier orbitals extend over the azadipyrromethene chromophore and the arylalkynyl substituents, with minimal involvement of zinc. Time-dependent DFT calculations indicate that the complexes' absorption of low-energy visible light results from four ligand-centered π–π^* states, where the alkynyl moieties act as electron donors to the azadipyrromethene core. The XRD structure shows intermolecular interactions in 3 dimensions and mobility measurements in both diode and transistor geometry demonstrate that charge transport is isotropic and ambipolar. $Zn(L1)_2$ and $Zn(L2)_2$ were tested in OPVs using P3HT as the donor and a PCE of 5.5% was obtained for $Zn(L2)_2$. The improved efficiency compared to $Zn(WS3)_2$ was explained by the improved electron mobility in blend films, good crystallinities of $Zn(L2)_2$ and P3HT, proper nanoscale phase separation and relatively low trap-assisted recombination. Compared to higher efficiency systems, the electron mobility of $Zn(L2)_2$ is relatively low, limiting the film thickness, photocurrent and FF. We are exploring other molecular modifications to deepen the energy levels and increase electron mobility. Further studies are required to better understand charge separation efficiency in these systems. $Zn(L2)_2$ was also found to have isotropic charge transport with high hole mobility. The electron donating properties of $Zn(L2)_2$ in a solar cell were demonstrated, making it a good candidate to pair with wide bandgap polymer electron acceptors with deep LUMO energy levels. The low synthetic complexity and industrial accessibility of $Zn(L2)_2$ have been demonstrated, showing that ADP-based zinc(II) complexes are an excellent platform to develop materials for OPVs.

Conflicts of interest

The authors declare no conflict of interest.

Acknowledgements

We are grateful to the National Science Foundation (CHEM 1148652 and CHEM 1904868) for funding this project. We thank Polyera Corporation for providing the polymer P(NDI2OD-T2), Muyuan Zhao for help with the device optimization, Dr John D. Protasiewicz for access to cyclic voltammetry instrumentation, and the Materials for Optoelectronics Research and Education (MORE) Center at CWRU for device fabrication and characterization. We thank Prof. Advincula at CWRU for access to his AFM instruments. This project was possible thanks to NSF MRI-0821515 for MALDI-TOF-TOF instrumentation and NSF MRI-1334048 for NMR instrumentation. This research utilized the 11-BM CMS beamline of the National Synchrotron Light Source-II (NSLS-II), Brookhaven National Laboratory (BNL), a U.S. Department of Energy User Facility operated for the Office of Science by BNL under contract No. DE-SC0012704. Computations at CWRU were supported by the U.S. Department of Energy, Office of Basic Energy Sciences, Division of Materials Science and Engineering, under Award DE-SC0010714 to T. G. G. This work made use of the High Performance Computing Resource in the Core Facility for Advanced Research Computing at CWRU.

References

1 G. Zhang, J. Zhao, P. C. Y. Chow, K. Jiang, J. Zhang, Z. Zhu, J. Zhang, F. Huang and H. Yan, *Chem. Rev.*, 2018, **118**, 3447–3507.

2 R. Xue, J. Zhang, Y. Li and Y. Li, *Small*, 2018, **14**, e1801793.

3 R. C. Chiechi, R. W. A. Havenith, J. C. Hummelen, L. J. A. Koster and M. A. Loi, *Mater. Today*, 2013, **16**, 281–289.

4 Y. Cui, H. Yao, J. Zhang, T. Zhang, Y. Wang, L. Hong, K. Xian, B. Xu, S. Zhang, J. Peng, Z. Wei, F. Gao and J. Hou, *Nat. Commun.*, 2019, **10**, 2515.

5 X. Li, F. Pan, C. Sun, M. Zhang, Z. Wang, J. Du, J. Wang, M. Xiao, L. Xue, Z.-G. Zhang, C. Zhang, F. Liu and Y. Li, *Nat. Commun.*, 2019, **10**, 1–11.

6 J. Yuan, T. Huang, P. Cheng, Y. Zou, H. Zhang, J. L. Yang, S. Y. Chang, Z. Zhang, W. Huang, R. Wang, D. Meng, F. Gao and Y. Yang, *Nat. Commun.*, 2019, **10**, 570.

7 K. Gao, S. B. Jo, X. Shi, L. Nian, M. Zhang, Y. Kan, F. Lin, B. Kan, B. Xu, Q. Rong, L. Shui, F. Liu, X. Peng, G. Zhou, Y. Cao and A. K. Jen, *Adv. Mater.*, 2019, **31**, e1807842.

8 J.-L. Wang, K.-K. Liu, L. Hong, G.-Y. Ge, C. Zhang and J. Hou, *ACS Energy Lett.*, 2018, **3**, 2967–2976.

9 W. Zhao, S. Li, H. Yao, S. Zhang, Y. Zhang, B. Yang and J. Hou, *J. Am. Chem. Soc.*, 2017, **139**, 7148–7151.

10 J. Yuan, Y. Zhang, L. Zhou, G. Zhang, H.-L. Yip, T.-K. Lau, X. Lu, C. Zhu, H. Peng, P. A. Johnson, M. Leclerc, Y. Cao, J. Ulanski, Y. Li and Y. Zou, *Joule*, 2019, **3**, 1140–1151.

11 S. Suman and S. P. Singh, *J. Mater. Chem. A*, 2019, DOI: 10.1039/c9ta08620j.

12 D. Rodriquez, S. Savagatrup, E. Valle, C. M. Proctor, C. McDowell, G. C. Bazan, T. Q. Nguyen and D. J. Lipomi, *ACS Appl. Mater. Interfaces*, 2016, **8**, 11649–11657.

13 S. Holliday, R. S. Ashraf, A. Wadsworth, D. Baran, S. A. Yousaf, C. B. Nielsen, C.-H. Tan, S. D. Dimitrov, Z. Shang, N. Gasparini, M. Alamoudi, F. Laquai, C. J. Brabec, A. Salleo, J. R. Durrant and I. McCulloch, *Nat. Commun.*, 2016, **7**, 11585.

14 W. Zhao, D. Qian, S. Zhang, S. Li, O. Inganas, F. Gao and J. Hou, *Adv. Mater.*, 2016, **28**, 4734–4739.

15 E. Y. Ko, G. E. Park, J. H. Lee, H. J. Kim, D. H. Lee, H. Ahn, M. A. Uddin, H. Y. Woo, M. J. Cho and D. H. Choi, *ACS Appl. Mater. Interfaces*, 2017, **9**, 8838–8847.

16 X. Du, T. Heumueller, W. Gruber, A. Classen, T. Unruh, N. Li and C. J. Brabec, *Joule*, 2019, **3**, 215–226.

17 R. Po, A. Bernardi, A. Calabrese, C. Carbonera, G. Corso and A. Pellegrino, *Energy Environ. Sci.*, 2014, **7**, 925–943.

18 R. Po, G. Bianchi, C. Carbonera and A. Pellegrino, *Macromolecules*, 2015, **48**, 453–461.

19 R. Po and J. Roncali, *J. Mater. Chem. C*, 2016, **4**, 3677–3685.

20 J. Min, Y. N. Luponosov, C. Cui, B. Kan, H. Chen, X. Wan, Y. Chen, S. A. Ponomarenko, Y. Li and C. J. Brabec, *Adv. Energy Mater.*, 2017, **7**, 1700465.

21 R. Lenaerts, T. Cardeynaels, I. Sudakov, J. Kesters, P. Verstappen, J. Manca, B. Champagne, L. Lutsen, D. Vanderzande, K. Vandewal, E. Goovaerts and W. Maes, *Sol. Energy Mater. Sol. Cells*, 2019, **196**, 178–184.

22 C. Sun, F. Pan, H. Bin, J. Zhang, L. Xue, B. Qiu, Z. Wei, Z. G. Zhang and Y. Li, *Nat. Commun.*, 2018, **9**, 743.

23 N. Li, I. McCulloch and C. J. Brabec, *Energy Environ. Sci.*, 2018, **11**, 1355–1361.

24 Z. Mao, W. Senevirathna, J. Y. Liao, J. Gu, S. V. Kesava, C. Guo, E. D. Gomez and G. Sauvé, *Adv. Mater.*, 2014, **26**, 6290–6294.

25 W. Senevirathna and G. Sauve, *J. Mater. Chem. C*, 2013, **1**, 6684–6694.

26 S. Pejić, A. M. Thomsen, F. S. Etheridge, R. Fernando, C. Wang and G. Sauvé, *J. Mater. Chem. C*, 2018, **6**, 3990–3998.

27 G. Sauve, *Chem. Rec.*, 2019, **19**, 1–16.

28 W. Senevirathna, J.-y. Liao, Z. Mao, J. Gu, M. Porter, C. Wang, R. Fernando and G. Sauvé, *J. Mater. Chem. A*, 2015, **3**, 4203–4214.

29 R. Fernando, S. Pejić, A. Thomsen, C. Wang and G. Sauvé, *Dyes Pigm.*, 2019, **168**, 257–263.

30 F. S. Etheridge, R. J. Fernando, S. Pejić, M. Zeller and G. Sauvé, *Beilstein J. Org. Chem.*, 2016, **12**, 1925–1938.

31 L. Gao, S. Tang, L. Zhu and G. Sauve, *Macromolecules*, 2012, **45**, 7404–7412.

32 M. Ozdemir, D. Choi, Y. Zorlu, B. Cosut, H. Kim, C. Kim and H. Usta, *New J. Chem.*, 2017, **41**, 6232–6240.

33 T. S. Teets, D. V. Partyka, J. B. Updegraff and T. G. Gray, *Inorg. Chem.*, 2008, **47**, 2338–2346.

34 T. S. Teets, D. V. Partyka, A. J. Esswein, J. B. Updegraff, M. Zeller, A. D. Hunter and T. G. Gray, *Inorg. Chem.*, 2007, **46**, 6218–6220.

35 T. S. Teets, J. B. Updegraff, A. J. Esswein and T. G. Gray, *Inorg. Chem.*, 2009, **48**, 8134–8144.

36 L. Gao, N. Deligonul and T. G. Gray, *Inorg. Chem.*, 2012, **51**, 7682–7688.

37 C. M. Proctor, M. Kuik and T.-Q. Nguyen, *Prog. Polym. Sci.*, 2013, **38**, 1941–1960.

38 M. M. Mandoc, W. Veurman, L. J. A. Koster, B. de Boer and P. W. M. Blom, *Adv. Funct. Mater.*, 2007, **17**, 2167–2173.

39 K. S. Nalwa, H. K. Kodali, B. Ganapathysubramanian and S. Chaudhary, *Appl. Phys. Lett.*, 2011, **99**, 263301.

40 C. Brabec, A. Cravino, D. Meissner, N. S. Sariciftci, T. Fromherz, L. Sanchez and J. C. Hummelen, *Adv. Funct. Mater.*, 2001, **11**, 374–380.

41 N. A. Unlu, S. O. Hacioglu, G. Hizalan, D. E. Yildiz, L. Toppare and A. Cirpan, *J. Electrochem. Soc.*, 2017, **164**, G71–G76.

42 F. Laquai, D. Andrienko, R. Mauer and P. W. Blom, *Macromol. Rapid Commun.*, 2015, **36**, 1001–1025.

43 Y. Liu, C. C. Chen, Z. Hong, J. Gao, Y. M. Yang, H. Zhou, L. Dou, G. Li and Y. Yang, *Sci. Rep.*, 2013, **3**, 3356.

44 J. Zhou, Y. Zuo, X. Wan, G. Long, Q. Zhang, W. Ni, Y. Liu, Z. Li, G. He, C. Li, B. Kan, M. Li and Y. Chen, *J. Am. Chem. Soc.*, 2013, **135**, 8484–8487.

45 C. Wang, Z. Zhang, S. Pejić, R. Li, M. Fukuto, L. Zhu and G. Sauvé, *Macromolecules*, 2018, **51**, 9368–9381.

46 T. Erb, U. Zhokhavets, G. Gobsch, S. Raleva, B. Stühn, P. Schilinsky, C. Waldauf and C. J. Brabec, *Adv. Funct. Mater.*, 2005, **15**, 1193–1196.

47 M.-Y. Chiu, U. S. Jeng, C.-H. Su, K. S. Liang and K.-H. Wei, *Adv. Mater.*, 2008, **20**, 2573–2578.

48 T. Mueller, R. Gresser, K. Leo and M. Riede, *Sol. Energy Mater. Sol. Cells*, 2012, **99**, 176–181.

49 M. Lorenz-Rothe, K. S. Schellhammer, T. Jaegeler-Hoheisel, R. Meerheim, S. Kraner, M. P. Hein, C. Schuenemann, M. L. Tietze, M. Hummert, F. Ortmann, G. Cuniberti, C. Koerner and K. Leo, *Adv. Electron. Mater.*, 2016, **2**, 1600152.

50 S. Y. Leblebici, L. Catane, D. E. Barclay, T. Olson, T. L. Chen and B. Ma, *ACS Appl. Mater. Interfaces*, 2011, **3**, 4469–4474.

51 Z. Li, J. D. A. Lin, H. Phan, A. Sharenko, C. M. Proctor, P. Zalar, Z. Chen, A. Facchetti and T.-Q. Nguyen, *Adv. Funct. Mater.*, 2014, **24**, 6989–6998.